Hindawi
International Journal of Chemical Engineering
Volume 2022, Article ID 1809835, 19 pages
https://doi.org/10.1155/2022/1809835

Research Article

Theoretical Analysis of Isentropic Exponent Effects on the Internal Flow of Supercritical CO_2 Centrifugal Compressors

Ben Zhao[1] and Zhiyuan Liu[2,3]

[1]*Institute of Engineering Thermophysics, Chinese Academy of Sciences, Beijing 100190, China*
[2]*School of Chemical Engineering and Energy Technology, Dongguan University of Technology, Dongguan 523808, China*
[3]*School of Energy and Power Engineering, Xi'an Jiaotong University, Xi'an 710049, China*

Correspondence should be addressed to Zhiyuan Liu; liuzhiyuan_ae@163.com

Received 4 February 2022; Revised 21 March 2022; Accepted 12 May 2022; Published 29 June 2022

Academic Editor: Maciej Jaskulski

The isentropic exponent in the near-critical region can sharply change with operation condition transitions of a closed Brayton cycle, thus having significant impacts on the compressor aerodynamic performance and the internal flow of the compressor embedded into the cycle. This paper investigates the isentropic exponent effects of the supercritical carbon dioxide (CO_2) using theoretical analyses and three-dimensional computational fluid dynamic (CFD) simulations. The theoretical analysis reveals that the increasing isentropic exponent mitigates the impeller work coefficient and the impeller outlet Mach number but raises the suction side Mach number of the impeller blade and blade loading at the leading edge. The CFD results provide validations for the theoretical results. Based on the findings, a suggestion is offered to guide the physical experiment design of a centrifugal compressor with supercritical CO_2 as its working fluid.

1. Introduction

The supercritical carbon dioxide (CO_2) Brayton cycle was proposed in the 1950s [1, 2]; however, it did not get much attention at that time. As global energy and environmental problems became serious, the supercritical CO_2 Brayton cycle has attracted more and more attention in the twenty-first century [3, 4]. Compared to the helium Brayton cycle and the conventional Rankine steam cycle, the same net efficiency can be achieved by a supercritical CO_2 cycle with a lower temperature and smaller size [5]. The compact heat exchangers and the turbomachinery of the supercritical carbon dioxide Brayton cycle have a good dynamic response to fast-varying loads and are beneficial to supply grid stability against dynamic changes [6]. This means that the supercritical CO_2 cycle is expected to replace the existing steam Rankine cycle in the future [7, 8]. Furthermore, the net efficiency of the supercritical CO_2 cycle had been proved to be significantly less sensitive to penalties from a core bypass flow and cycle pressure drops than the helium Brayton cycle [9]. With those advantages, the supercritical CO_2 Brayton cycle is considered to be most promising in the fields of waste heat utilization, solar thermal power generation, nuclear energy, and so on [10, 11].

Compression is one of the critical processes in a supercritical CO_2 cycle, greatly influencing both the cycle system performance and stability. As one of the compression devices, the centrifugal compressor has the advantages of high single-stage pressure ratio, flow stability, compactness, cheapness, etc. Our previous research showed that the centrifugal compressor is the most suitable type of compression component in a 1–100 MWe supercritical CO_2 Brayton cycle power generation system [12, 13]. A literature survey reported by [14, 15] revealed that most of the existing supercritical CO_2 experimental rigs adopted the centrifugal type as the compression component.

Compared with air compressors, the period of supercritical CO_2 centrifugal compressor investigation is much shorter. A hot concern in the supercritical CO_2 compressor development is how the real-gas properties affect the

compressor flow field and performance. Understanding the real gas effect is of importance because it can help design a better supercritical CO_2 compressor. Besides solving the design issue, it can also provide guidelines for a similar model test under a condition with lower pressure and/or other gas using an accurate similarity theory. After all, the pressure higher than the CO_2 critical pressure (7.38 MPa) is still a great challenge for most laboratories over the world. Therefore, it is of necessity to investigate the real-gas effects of supercritical CO_2 on a centrifugal compressor.

Focusing on a few dimensionless parameters is the most important means to study flow similarity. According to the dimensional analysis method, the operating characteristics of the compressor can be described by the following dimensionless equation (16).

$$\eta, \frac{\Delta h_0}{U_2^2} = f\left(\frac{4\dot{m}}{\pi\rho_0 U_2 D_2^2}, \frac{U_2}{a_0}, \frac{\rho_0 U_2 D_2}{\mu_0}, n_s\right) = f\left(\phi, Ma_M, \mathrm{Re}_M, n_s\right). \quad (1)$$

The first term at the right side of the equation is the flow coefficient; the second one stands for the machine Mach number; the third one represents the machine Reynolds number; the fourth one corresponds to the isentropic exponent. Once all the dimensionless parameters are the same, the internal flow field should be similar. The isentropic exponent is constant for an ideal gas. Formula (1) indicates that as long as the machine Mach number and machine Reynolds number are the same, the compressor performance having an ideal gas as its working fluid is only related to the flow coefficient. Unlike the ideal gas, the isentropic exponent varies for a real gas; thus, it is hard to guarantee if the compressor performance will be the same. This is referred to as the effects of the real-gas properties. Formula (2) describes the isentropic exponent.

$$n_s = \frac{c_p/cv}{\beta_T p} = \frac{\gamma}{\beta_T p}. \quad (2)$$

where γ stands for the well-known ratio of specific heats. For ideal gases, γ can be seen as a constant. Figure 1 shows the variation of the isentropic exponent under different supercritical CO_2 compressor inlet conditions. It can be seen that the isentropic exponent changes rapidly in the liquid-like region. In contrast, the change is relatively small in the gas-like region. Unfortunately, it is hard to avoid the fluid parameter fluctuation at a compressor inlet for a closed cycle experiment. In other words, the compressor inlet condition hardly remains constant in a closed cycle. The white box in Figure 1 represents the test operation range of the Sandia CO_2 compressor [17]. The plot indicates that the isentropic exponent at the compressor inlet changes significantly between the testing operation points.

Many researchers have focused on the real-gas effects of CO_2. Monje et al. compared the performance of supercritical CO_2 (315 K, 95 bar) against air in a conical diffuser by numerical simulations [18]. The results showed that the

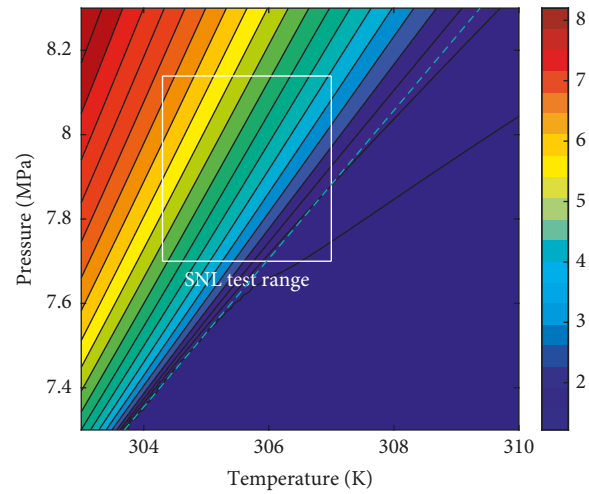

Figure 1: Isentropic exponent of CO_2 in the near-critical region.

supercritical CO_2 has a higher static pressure rise coefficient under the same inlet Mach number, blockage factor, and turbulence intensity. In addition, the numerical simulations showed that supercritical CO_2 is more sensitive to the expansion angle (area ratio) of the diffuser than air, which means that the real-gas properties make the fluid behave differently under the reverse pressure gradient. Tello et al. [19] utilized the same method as Monje et al. [18] to compare the flow of air and supercritical CO_2 (314.6 K, 75.236 bar) in a two-dimensional cascade. However, the intake conditions of these studies are far from the critical point (304.13 K, 7.38 MPa).

Baltadjiev et al. analyzed the real-gas effects near the critical point on the supercritical CO_2 flow [20]. It was pointed out that the isentropic exponent reflected the degree of deviation from the ideal gas. The results presented that increasing the isentropic exponent would lead to a choking mass flow reduction. Moreover, the numerical simulation results of a two-dimensional impeller also confirm the reduction in the chocking flow capacity. The mechanism contributing to the flow capacity reduction is the increased isentropic exponent near the critical point. Baltadjiev had concluded that the isentropic exponent is the key parameter to determine the ideal gas and the real-gas dynamics. Recently, a few researchers (such as Romei et al. [21], Pham et al. [22], and Jeong et al. [23]) confirmed the conclusion that the same isentropic exponent is an indispensable condition for guaranteeing the similarity conditions.

Although the isentropic exponent has played a vital role in compressor flow similarity and performance map, there is still no quantitative assessment of the real-gas properties in the existing research. The qualitative influence of the isentropic exponent on the performance map is also seldom understood. This work investigates the effects of the isentropic exponent on a supercritical CO_2 compressor flow field and performance map and reports a few quantitative results. Unlike previous studies, a combination of theoretical and numerical investigations in this paper ensures the conclusion is generalizable. Section 2 presents the theoretical

analysis of isentropic exponent effects. Section 3 introduces the 3-D computational fluid dynamic (CFD) method and its validation. With the CFD approach, a cases study is carried out in Section 4 and Section 5 validates the conclusion from the theoretical analysis.

2. Theoretical Analysis of Isentropic Exponent Effects

Though past investigations have proved the existence of isentropic exponent effects, few of them give a detailed theoretical explanation. This section analyzes the relationship between the flow behavior and the isentropic exponent using aerodynamics prediction. The results could be generalizable since the theoretical analysis does not depend on any specific compressor.

2.1. Effects on the Density and Pressure. Depending on the nonlinear equations in Appendix A, once the inlet parameters and the machine Mach number are defined, the influence of isentropic exponent on density and pressure can be determined by the following equations.

$$\frac{\rho_x}{\rho_0} = \left[1 + \frac{n_s - 1}{2}\left(\frac{U_x}{U_2}\right)^2 Ma_M^2 - \frac{n_s - 1}{2} Ma_x^2 \left(1 + \frac{n_s - 1}{2} Ma_x^2 - \frac{n_s - 1}{2} Ma_{ux}^2\right)^{-1}\right]^{1/(n_s - 1)}, \tag{3}$$

$$\frac{P_x}{P_0} = \left[1 + \frac{n_s - 1}{2}\left(\frac{U_x}{U_2}\right)^2 Ma_M^2 - \frac{n_s - 1}{2} Ma_x^2 \left(1 + \frac{n_s - 1}{2} Ma_x^2 - \frac{n_s - 1}{2} Ma_{ux}^2\right)^{-1}\right]^{n_s/(n_s - 1)}, \tag{4}$$

$$\frac{Ma_{ux}}{Ma_M} = \frac{U_x}{U_2}\left(1 + \frac{n_s - 1}{2} Ma_x^2 - \frac{n_s - 1}{2} Ma_{ux}^2\right)^{1/2}. \tag{5}$$

Combining equations (3), (4), and (5) makes it possible to calculate the local dimensionless density and the dimensionless static pressure. In the following analyses, the value of U_{s1}/U_2 and Ma_M are 0.5016 and 0.681, respectively.

Figure 2 shows the relationship of local density/pressure and the local Mach number at the impeller inlet tip ($U_x = U_{s1}$). For the density diagram (shown in Figure 2(a)), the deviation between different isentropic exponent values is negligible when the local Mach number is not too high. A conclusion can be drawn that, for the subsonic cases, the isentropic exponent has an insignificant impact on the dimensionless density.

Unlike the dimensionless density, the isentropic exponent can significantly influence the dimensionless pressure. For instance, in Figure 2(b), we can see a significant deviation between different isentropic exponent values when the isentropic exponent is greater than 3. Specifically, a high isentropic exponent value always corresponds to a higher dimensionless static pressure in the Mach number below 0.35. In contrast, it accompanies a lower dimensionless static pressure in the Mach number range higher than 0.35.

According to equations (A.6)–(A.8) in Appendix A, Figure 3 shows the isentropic exponent effects of real gas on the dimensionless density and pressure. Comparing Figure 3 against Figure 2 reveals that the constant isentropic exponent can qualitatively reflect the influence of the real-gas isentropic exponent on its gas dynamic behavior.

At the impeller exit ($U_x = U_2$), the isentropic exponent effects on the dimensionless density and the dimensionless pressure are more remarkable. For the density diagram (shown in Figure 4(a)), when the relative Mach number is less than 0.5, a large isentropic exponent value always corresponds to a low dimensionless density value. Unlike the inlet analysis, there is no crossing point between those lines for the pressure diagram (shown in Figure 4(b)). So, it is concluded that a large isentropic exponent value always matches a high dimensionless static pressure.

2.2. Effects on the Impeller Outlet Mach Number. If the diffuser channel can be simplified as a one-dimensional pipe, we can introduce the continuity equation of pipe flow as follows:

$$\begin{aligned} q_m = \rho_3 A_3 V_3 \cos\beta_3 &= \frac{\left(1 + (n_s - 1)/Ma_3^2\right)^{-1/(n_s - 1)} P_{0,3}}{R_g T_{0,3}}, \\ &A_3\left[n_s R_g T_{0,3}\left(1 + \frac{n_s - 1}{2} Ma_3^2\right)^{-1}\right]^{1/2}, \\ &Ma_3 \cos\beta_3 = \left(1 + \frac{n_s - 1}{2} Ma_3^2\right)^{-1/(n_s - 1) - (1/2)}, \\ &Ma_3 P_{0,3}\sqrt{\frac{n_s}{R_g T_{0,3}}} A_3 \cos\beta_3. \end{aligned} \tag{6}$$

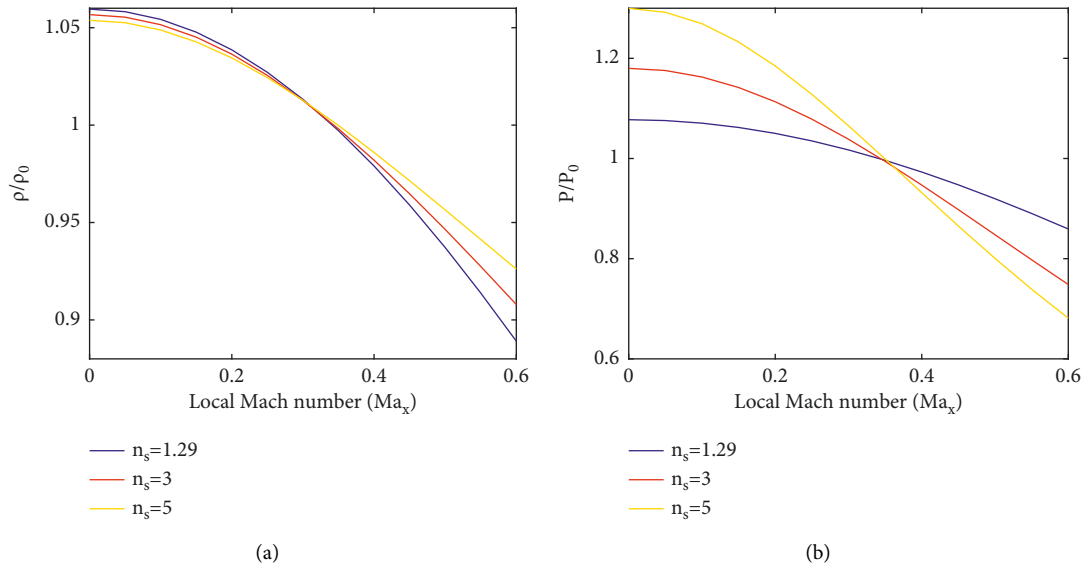

Figure 2: Isentropic exponent effects at the inlet tip of the impeller. (a) Density and (b) pressure.

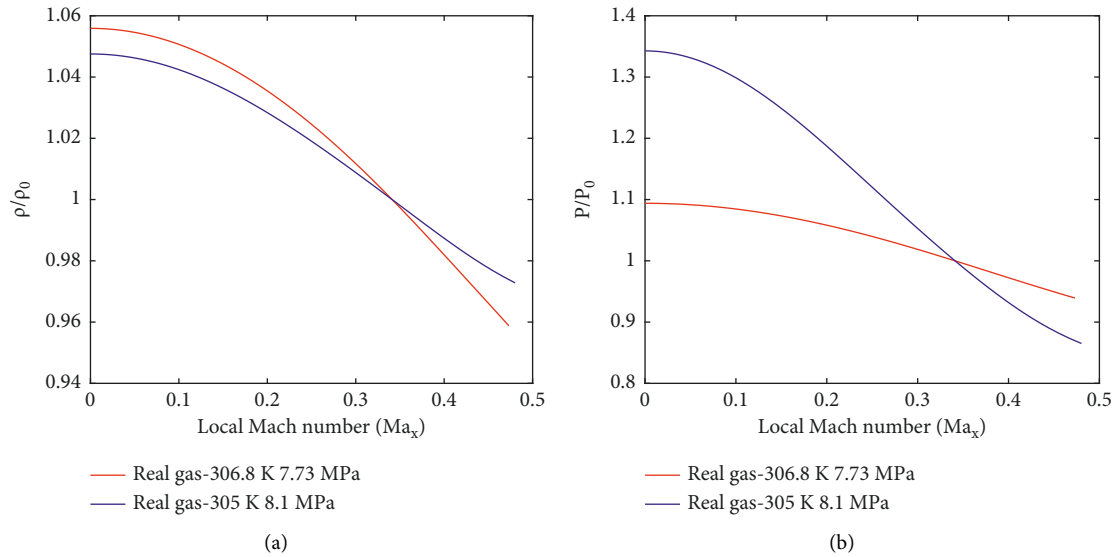

Figure 3: Real-gas cases with variable isentropic exponents at the inlet tip of the impeller. (a) Density and (b) pressure.

Once the flow area at any section $A_x = A_x\,(r)$ is known, we can calculate the Mach number and velocity at an arbitrary position in the diffuser.

$$\left(1+\frac{n_s-1}{2}Ma_3^2\right)^{-(n_s+1)/(2n_s-2)},$$

$$Ma_3A_3\cos\beta_3=\left(1+\frac{n_s-1}{2}Ma_x^2\right)^{-(n_s+1)/(2n_s-2)}, \quad (7)$$

$$Ma_xA_x\cos\beta_x.$$

From the above equation, it can be concluded that the local Mach number is only dependent on the inlet Mach number and the isentropic exponent. Figure 5 illustrates the result of equation (7). When the inlet Mach number is higher than 0.2, the increasing isentropic exponent drops an outlet Mach number.

For impellers, based on the discussion in Appendix B, the isentropic exponent effects of a real gas on the impeller outlet Mach number can be obtained by the following equations.

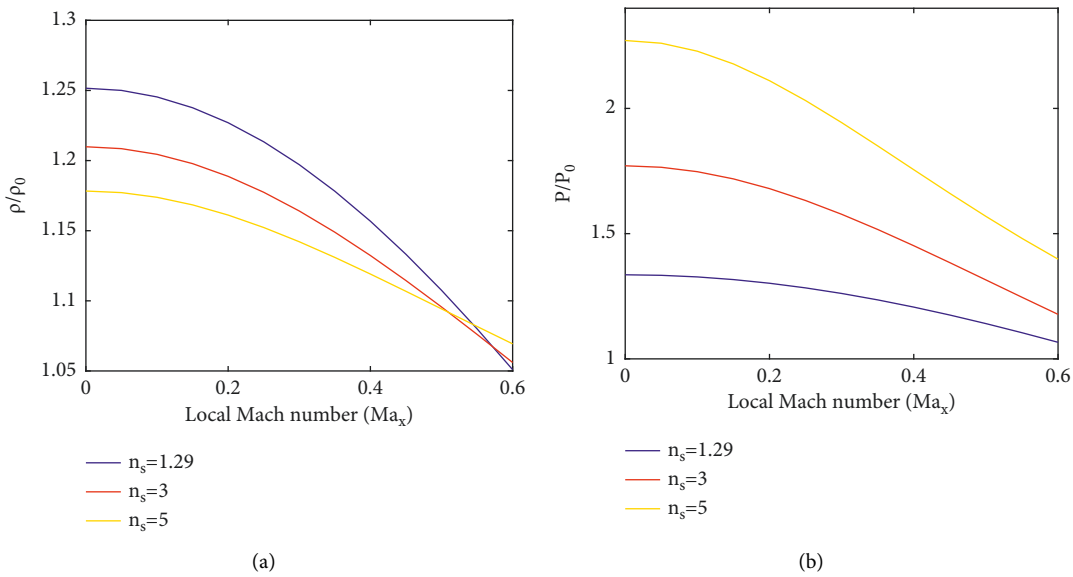

Figure 4: Isentropic exponent effects at the impeller outlet. (a) Density and (b) pressure.

$$\frac{Ma_x}{Ma_{1,m}} = \frac{W_x/W_{1,m}}{a_x/a_{1,m}}, \tag{8}$$

$$\frac{W_x}{W_{1,m}} = \frac{A_1}{A_x}\frac{\cos\beta_{1,m}}{\cos\beta_x}\left[1 + (n_s - 1)\frac{1 - \left(W_x/W_{1,m}\right)^2}{2}Ma_{1,m}^2 + (n_s - 1)\frac{\left(U_x/U_{1,m}\right)^2 - 1}{2}Ma_{u1,m}^2\right]^{-1/(n_s-1)}, \tag{9}$$

$$\frac{a_x}{a_{1,m}} = \left[1 + (n_s - 1)\frac{1 - \left(W_x/W_{1,m}\right)^2}{2}Ma_{1,m}^2 + (n_s - 1)\frac{\left(U_x/U_{1,m}\right)^2 - 1}{2}Ma_{u1,m}^2\right]^{1/2}, \tag{10}$$

$$\frac{Ma_{u1,m}}{Ma_M} = \frac{U_{1,m}}{U_2}\left(1 + \frac{n_s - 1}{2}Ma_{1,m}^2 - \frac{n_s - 1}{2}Ma_{u1,m}^2\right)^{1/2}, \tag{11}$$

$$\phi = \frac{4\dot{m}}{\pi\rho_0 D_2^2 U_2} = \frac{D_{s1}^2 - D_{h1}^2}{D_2^2}\frac{\rho_1}{\rho_0}\frac{W_{1,m}}{U_2}\cos\beta_{1,m} = \frac{D_{s1}^2 - D_{h1}^2}{D_2^2}\frac{Ma_{1,m}}{Ma_M}\frac{\rho_1}{\rho_0}\frac{a_1}{a_0}\cos\beta_{1,m}. \tag{12}$$

The number of unknown variables (Ma_x, $Ma_{1,m}$, $Ma_{u1,m}$, $W_x/W_{1,m}$, and $a_x/a_{1,m}$) is equal to that of equations. When the inlet flow coefficient and local area are fixed, the local Mach number will be determined according to equations (8)–(12). Figure 6 shows the result at the impeller outlet.

Figure 6 reveals that the increase of isentropic exponent value reduces the relative Mach number at the impeller outlet, similar to the diffuser analysis.

2.3. Effects on the Impeller Work Coefficient. The variation of the outlet Mach number will lead to the change of impeller loading. According to the Euler equation, the work coefficient can be expressed as follows:

$$\psi = \frac{\Delta h_0}{U_2^2} == 1 - \frac{W_2\sin\beta_2}{U_2} = 1 - \frac{Ma_2\sin\beta_2}{Ma_{u2}}. \tag{13}$$

$$\frac{Ma_{u2}}{Ma_M} = \left(1 + \frac{n_s - 1}{2}Ma_2^2 - \frac{n_s - 1}{2}Ma_{u2}^2\right)^{1/2}. \tag{14}$$

The calculating process of Ma_2 has been introduced in Section 2.2. Based on equations (13) and (14), Figure 7 shows the relationship between the work coefficient and the flow coefficient with different isentropic exponent values. The increase of the isentropic exponent reduces the work

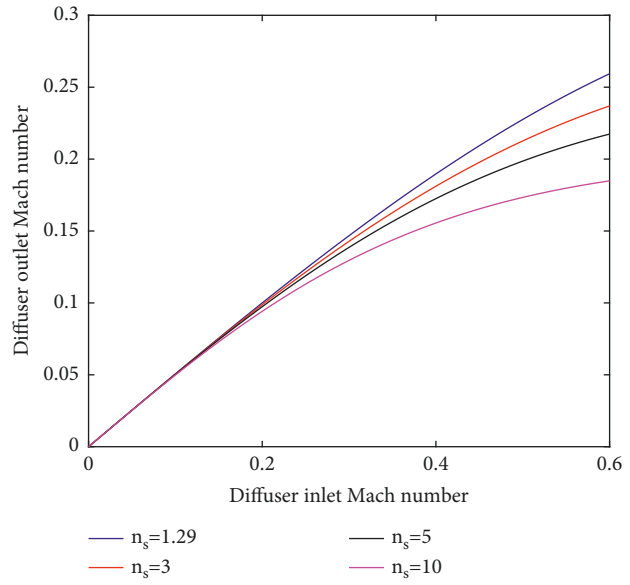

Figure 5: Isentropic exponent effects on the diffuser outlet Mach number.

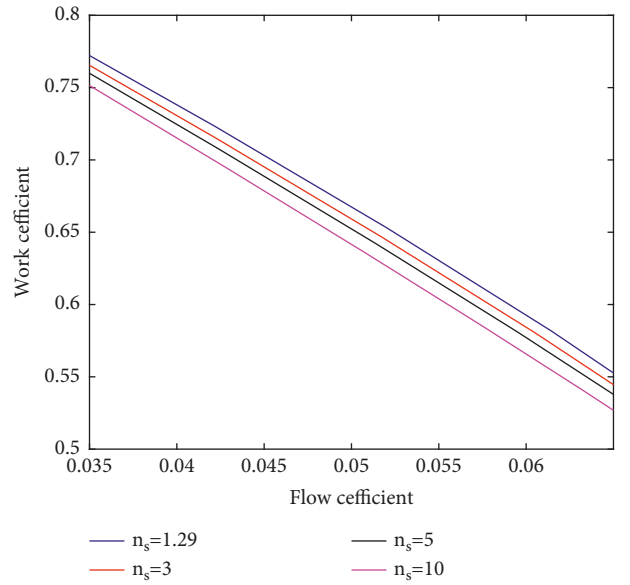

Figure 7: Isentropic exponent effects on the impeller work coefficient.

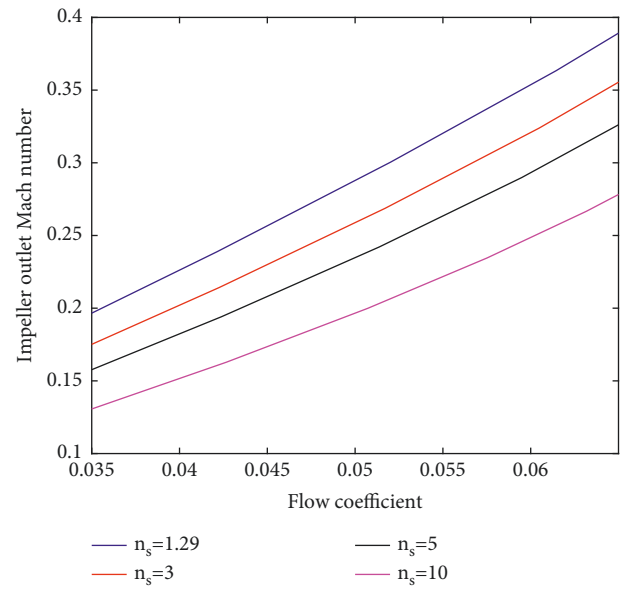

Figure 6: Isentropic exponent effects on the impeller outlet Mach number.

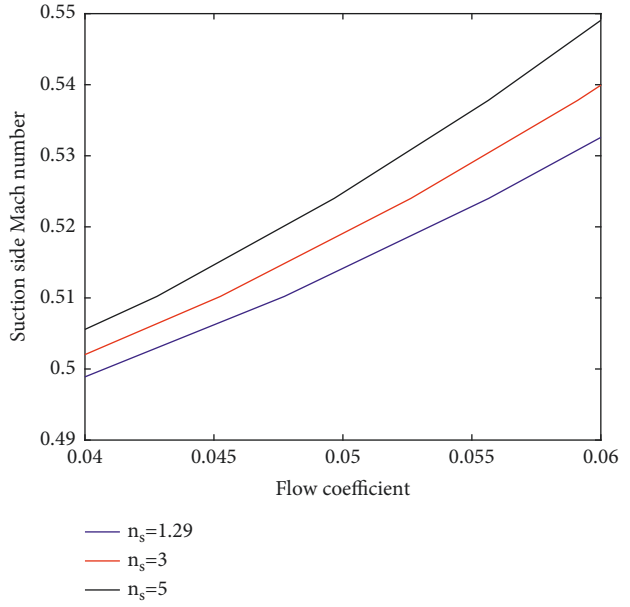

Figure 8: Isentropic exponent effects on the Mach number at the impeller suction side.

coefficient. The predicted effect is consistent with the past CFD results of Romei et al. [22]. The consistency gives more confidence to our analysis.

2.4. Leading Edge Mach Number. According to the equations in Appendix C, the Mach number of the suction side at the blade leading edge can be obtained with different isentropic exponent values as displayed in Figure 8. The larger the isentropic exponent is, the higher the Mach number is.

$$Ma_{1t,s} = Ma_{1t}\left(1 - \frac{r\,d\beta}{2\,dm}\Big|_{1t}\Delta\theta_1\right), \tag{15}$$

$$Ma_{1t,p} = Ma_{1t}\left(1 + \frac{r\,d\beta}{2\,dm}\Big|_{1t}\Delta\theta_1\right), \tag{16}$$

$$\frac{Ma_{u1t}}{Ma_M} = \frac{U_{1t}}{U_2}\left(1 + \frac{n_s - 1}{2}Ma_{1,t}^2 - \frac{n_s - 1}{2}Ma_{u1t}^2\right)^{1/2}, \tag{17}$$

$$Ma_{z1} = \sqrt{Ma_{1t}^2 - Ma_{u1t}^2}, \tag{18}$$

$$\phi = \frac{4m}{\pi\rho_0 D_2^2 U_2} = \frac{D_{s1}^2 - D_{h1}^2}{D_2^2}\left(1 + \frac{n_s - 1}{2} Ma_{z1}^2\right)^{-1/(n_s-1)} \frac{Ma_{z1}}{Ma_M}\frac{a_1}{a_0}. \tag{19}$$

2.5. Blade Loading. Blade loading distribution is one of the key factors to determine the centrifugal compressor performance [24, 25] because the loading distribution directly determines both leakage flow loss and compressor stall margin. This part investigates the isentropic exponent effects on the blade loading. The blade loading is judged by the ratio of static pressure values on two sides of a blade.

Since the relative total pressure of the suction surface and pressure surface is equal, the relationship between the static pressure ratio and flow coefficient at the impeller inlet tip can be expressed as follows:

$$\frac{p_{1t,s}}{p_{1t,p}} = \frac{\left(1 + (n_s - 1)/2Ma_{1t,s}^2\right)^{(-n_s)/(n_s-1)}}{\left(1 + (n_s - 1)/2Ma_{1t,p}^2\right)^{(-n_s)/(n_s-1)}}. \tag{20}$$

The calculating process of $Ma_{1t,s}$ and $Ma_{1t,p}$ has been introduced in Section 2.4. According to equation (20), the static pressure ratio at the leading edge is presented in Figure 9. We can conclude that the larger the isentropic exponent value is, the higher the blade loading is.

At the impeller outlet, $\sin\gamma = 1$; thus, $dm = dr/\sin\gamma = dr$ and$r = r_2\tilde{r}$. Thus, the relative velocity difference at the impeller outlet can be obtained.

$$\frac{\Delta W_2}{W_2} = 2\frac{U_2}{W_2}\cos\beta_2\Delta\theta_2 - \frac{d\beta}{d\tilde{r}}\Delta\theta|_2 = 2\frac{Ma_{u2}}{Ma_2}\cos\beta_2\Delta\theta_2 - \frac{d\beta}{d\tilde{r}}\Delta\theta|_2. \tag{21}$$

Similar to the impeller inlet, the Mach number of the impeller outlet blade surface is listed as follows:

$$Ma_{2,s} = Ma_2\left(1 + \frac{Ma_{u2}}{Ma_2}\cos\beta_2\Delta\theta_2 - \frac{d\beta}{2\,d\tilde{r}}\Delta\theta|_2\right), \tag{22}$$

$$Ma_{2,p} = Ma_2\left(1 - \frac{Ma_{u2}}{Ma_2}\cos\beta_2\Delta\theta_2 + \frac{d\beta}{2\,d\tilde{r}}\Delta\theta|_2\right). \tag{23}$$

According to the conservation of rothalpy, the relative stagnation pressure on both sides of a blade with the same radius is equal, thus:

$$\frac{p_{2,s}}{p_{2,p}} = \frac{\left(1 + (n_s - 1)/2Ma_{2,s}^2\right)^{-n_s/(n_s-1)}}{\left(1 + (n_s - 1)/2Ma_{2,p}^2\right)^{-n_s/(n_s-1)}}. \tag{24}$$

Figure 10 depicts the relationship between the static pressure ratio and the flow coefficient at the impeller outlet. A large isentropic exponent value corresponds to a high blade loading, similar to the impeller inlet.

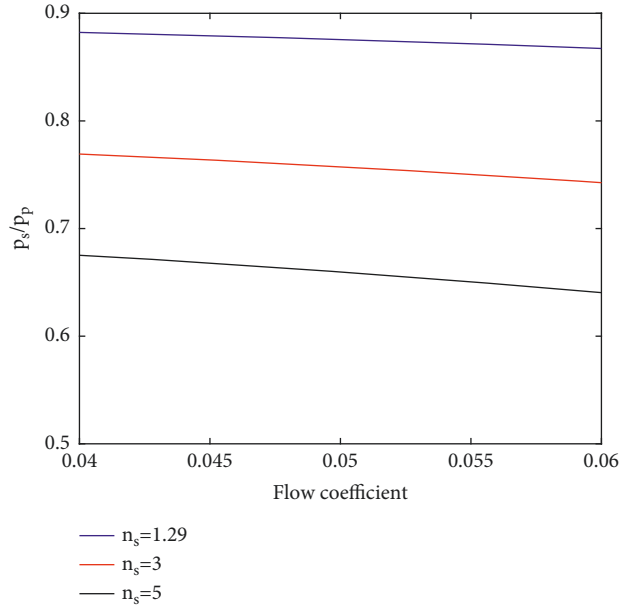

Figure 9: Static pressure ratio at the tip of the impeller leading edge.

In summary, increasing the exponent value reduces the working coefficient. As for the impeller flow field, the increase in isentropic exponent raises the Mach number and blade loading at the leading edge of the impeller blade, but mitigates the Mach number at the impeller passage outlet.

3. Numerical Method

3.1. Numerical Model. The compressible Reynolds-averaged Navier–Stokes (RANS) equations were solved using a commercial finite volume method solver embedded in the NUMECA Fine/Turbo software package with a version of 11.2. To achieve the closure of the governing equations, Menter's SST turbulence model was adopted to solve the turbulent flows since it has good applicability for both separated flow and inverse pressure gradient flow, especially in a centrifugal compressor [26]. All the wall surfaces are defined with the adiabatic condition and a mean roughness of 1.6 μm. To meet the near-wall requirements of the turbulence model, the minimum grid spacing on solid walls was set to be less than 1×10^{-6} m. Given the current maximum $y+$ value lower than 50, the extended wall function was employed for the ω-based turbulence model. Moreover, data transfer between the impeller and diffuser domains used Denton' mixing-plane approach [27]. The second-order central difference scheme is adopted for the inviscid flux calculation. The multigrid strategy and implicit residual smoothing method are used to accelerate convergences.

For the boundary conditions of the computational domain, the total temperature and total pressure specified at the inlet are displayed in Table 1. The inlet flow was assumed to be in the axial direction, i.e., the flow angle is 0°. As for the exit boundary condition, the average static pressure boundary condition at the vaned diffuser exit was adopted and the pressure profile was obtained by extrapolation from

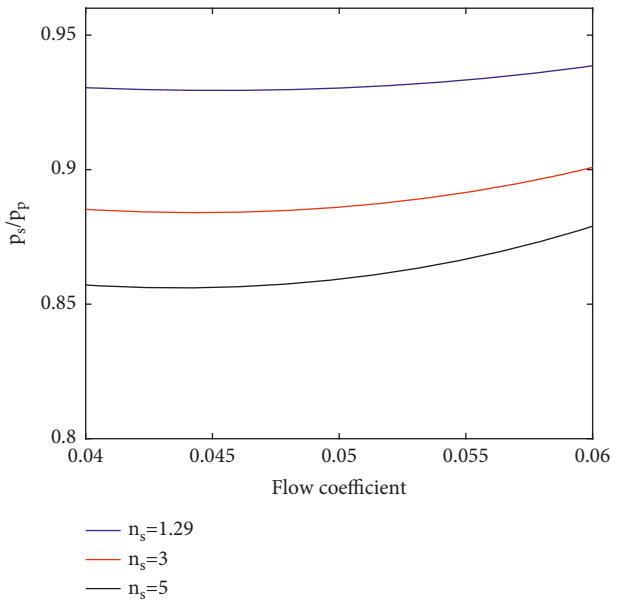

Figure 10: Static pressure ratio at the impeller outlet.

Table 1: Design specification of the SNL compressor [30, 31].

Inlet shroud radius (mm)	9.372	Tip clearance (mm)	0.254
Inlet hub radius (mm)	2.5375	Blade thickness (mm)	0.762
Exit blade height (mm)	1.712	Number of diffuser vanes	17
Exit blade radius (mm)	18.6817	Exit blade back sweep angle	50°
Number of all blades	6 + 6	Inlet blade angle at tip	50°

the interior field. The central difference scheme was used for the spatial discretization, and the local time-stepping method was employed.

To take the real-gas behavior of the working fluid into account, the real-gas properties' tables are generated through the equation of state of the Span and Wagner type and are used to interpolate the CO_2 properties during the CFD simulations. The thermodynamic property table ranges were 250–600 K with 301 nodes for temperature and 1–30 MPa with 301 nodes for pressure. The resolution of the physical property table is enough to meet the table independence requirement according to the investigations of Li et al. [28] and Saxena et al. [29].

3.2. Model Validation. The supercritical CO_2 centrifugal compressor tested by the Sandia National Laboratories (SNL) and a megawatt-scale supercritical CO_2 centrifugal compressor tested by the Institute of Engineering Thermophysics in the Chinese Academy of Sciences (IET-CAS) are modeled and adopted as the research objects. The reason for the selection is that the compressors' geometric parameters and performance curve had been reported in literature [30–32]. The specification of the SNL compressor is displayed in Table 1.

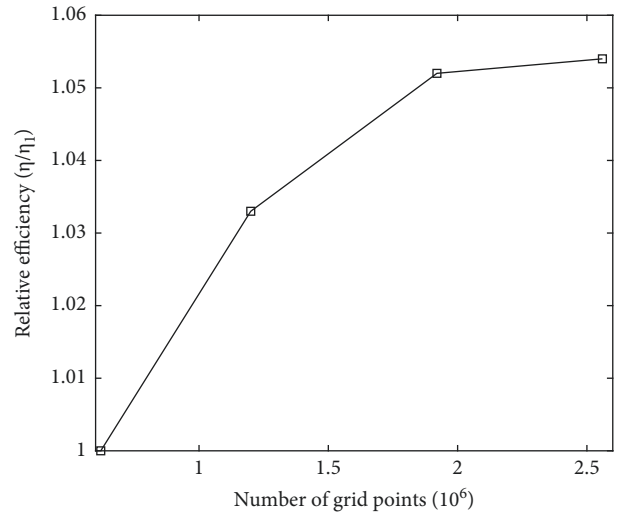

Figure 11: Grid sensitivity of the SNL supercritical CO_2 centrifugal compressor.

The SNL supercritical CO_2 impeller contains 6 main blades and 6 splitter blades. Its diffuser has 17 wedge-shaped vanes. To reduce computing expense, a single blade passage was chosen as the computational domain. The structured grid was generated using the periodic multiblock O4H-type structured grid. A mesh independence investigation is conducted to eliminate the influence of node number on numerically predicted results as displayed in Figure 11.

Figure 12 shows the computational mesh. The total number of grid nodes was 1.92 million and had been proved to meet the requirement of this research work by carrying out the cell-size sensitivity analysis. In addition, Raman et al. [33] and Ameli et al. [34] had done a similar study on the cell size. Their results can provide support for the node number used in this research.

The design inlet conditions of the SNL compressor are 305.372 K and 7687.925 kPa. As reported, the supercritical CO_2 compressor inlet conditions in tests varied within 304.3–307 K and 7700–8139 kPa. SNL has utilized the Glassman method [35] to obtain the corrected performance based on the actual temperature and pressure under the design condition. The definition of Glassman's dimensionless parameters is listed as follows.

$$\dot{m}_{ad} = \frac{m\sqrt{\gamma r Z_{cr} T_{cr}}}{\gamma P_{cr}}, \tag{25}$$

$$N_{ad} = \frac{ND_2}{\sqrt{\gamma r Z_{cr} T_{cr}}}, \tag{26}$$

$$\Delta h_{0,ad} = \frac{\Delta h_{0,s}}{\gamma r Z_{cr} T_{cr}}, \tag{27}$$

$$Z_{cr} T_{cr} = Z_0 T_0 \left(\frac{1+\gamma}{2}\right)^{-1}, \tag{28}$$

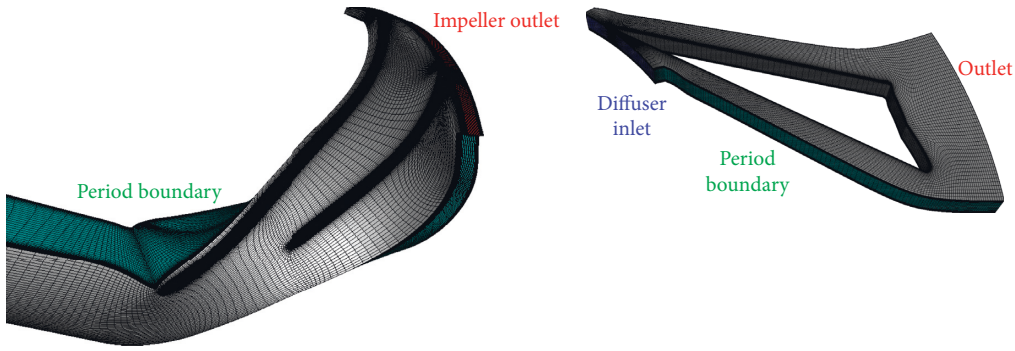

Figure 12: Computational grid of the SNL compressor. (a) Impeller mesh and (b) vaned diffuser mesh.

Table 2: Validation case operating conditions.

Operation condition	T_0	P_0	Actual speed	N_{ad}
Low rotating speed	305.372 K	7687.925 kPa	45000 RPM	10.63
High rotating speed	305.372 K	7687.925 kPa	50000 RPM	11.8

Table 3: List of adopted loss models.

Classification of loss type	Loss models
Volute loss	Zhu and Sjolander [36]
Leakage loss	Aungier [37]
Recirculation loss	Oh et al. [38]
Disk friction loss	Daily and Nece [39]

$$P_{cr} = P_0\left(\frac{1+\gamma}{2}\right)^{-\gamma/(\gamma-1)}. \quad (29)$$

Based on the tested conditions of the SNL compressor, the simulation conditions of the validating case were determined and introduced in Table 2. The dimensionless speed N_{ad} is kept the same with experimental conditions in the current comparison.

It should be noted that the compressor configuration in the experiment has a volute. In our study, however, the volute was neglected. Besides, the CFD simulation did not include parasitic losses, consisting of leakage loss, recirculation loss, and disk friction loss. To account for the volute and parasitic losses, the compressor performance is recalculated with the calculating models as displayed in Table 3 and then compared with experimental data for validating the CFD simulations to some degree.

On the above basis, the revised compressor efficiency can be expressed as follows:

$$\eta_{\text{revised}} = \frac{M\cdot\omega\cdot\eta - \Delta h_{\text{volute}}}{M\cdot\omega + \Delta h_{\text{leakage}} + \Delta h_{\text{recirculation}} + \Delta h_{\text{disk}}}. \quad (30)$$

Figure 13 shows the comparison of the compressor performance with experimental data from SNL [31]. All the data have been nondimensionalized with the Glassman method, which ensures the data processing method to be the same as the SNL. The definition of the dimensionless parameters is introduced in equations (25)–(29).

In Figure 13, the deviations between CFD and experimental results should be acceptable, not only based on efficiency but also enthalpy rise. The good agreement gives confidence to the numerical simulation method. The following section investigates the isentropic exponent effects on the flow similarity of supercritical CO_2 centrifugal compressors with the current numerical scheme.

The IET megawatt-scale supercritical CO_2 centrifugal compressor consists of an intake pipe, an impeller, a vaneless diffuser, and a volute. The impeller has 15 blades. Different from the Sandia compressor, the IET compressor employs a vaneless diffuser, thus never having a strong rotor-stator interaction. Table 4 lists its main geometric parameters.

The diagram and development of the supercritical CO_2 test rig in the IET-CAS can be found in Zhu's Doctoral dissertation [32]. The total temperature and pressure at the inlet of the compressor were 309.4 K and 7.827 MPa, respectively. The corresponding rotating speed is 34500 RPM. A HO topology pattern is employed for the impeller part. Specifically, an O-type block is used around the blade and four H-type blocks are applied inside the B2B channel. As for the blade tip clearance, 4 H-type blocks surrounded by an O-type block are utilized. The mesh near the leading edge and trailing edge of the impeller is locally refined by using "add Z Constant Line" of Autogrid software as displayed in Figure 14.

A mesh independence investigation is validated to eliminate the influence of node number on numerically predicted results as shown in Figure 15. It depicts that the grid independence requirement is met when the number of grid nodes is greater than 0.89 million. 17 grid points are specified along the span-wise direction inside the tip clearance for the final computational mesh.

Figures 16(a) and 16(b) describe the compressor efficiency and work coefficient as a function of the flow coefficient, respectively. The definitions of the flow coefficient, actual efficiency, and work coefficient are introduced in equations (31) and (32). To account for the effect of volute, the compressor performance is revised with the volute loss model [36].

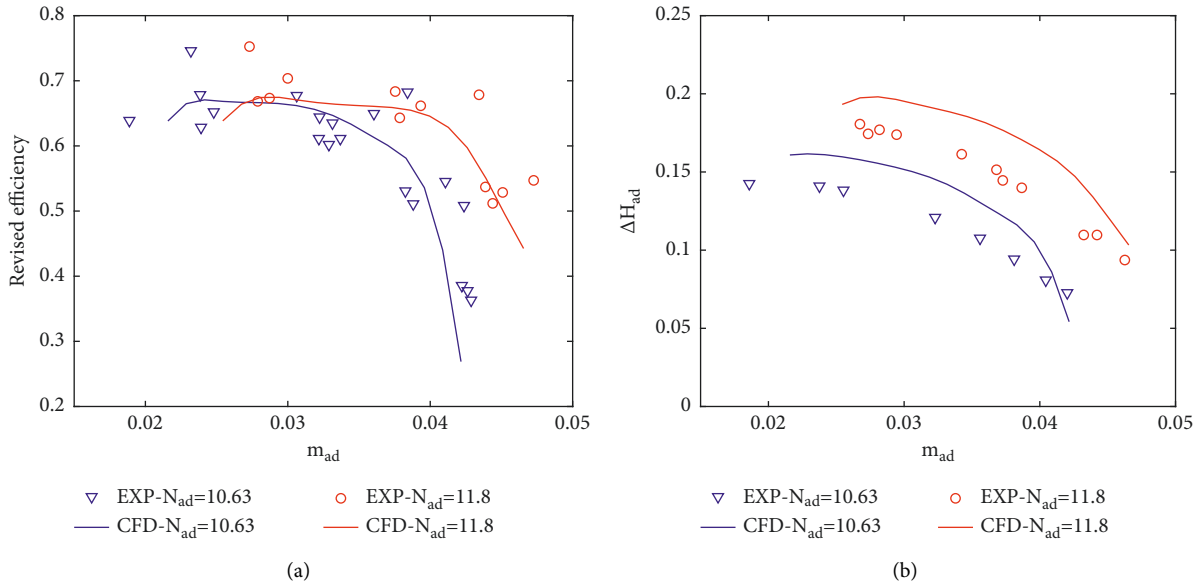

Figure 13: Comparison of numerically predicted results against the SNL experimental data. (a) Revised efficiency and (b) Glassman enthalpy rise.

Table 4: Design specification of the IET impeller [32].

Item	Value	Item	Value
Blade number	15	Split blade number	0
Hub diameter	20 mm	Outlet blade height	3.5 mm
Impeller diameter	96 mm	Blade angle at inlet	60°/48°
Inlet blade height	7.5 mm	Blade angle at outlet	50°
Shroud diameter	40 mm	Blade thinness	1.5 mm
Tip clearance	0.45 mm	Reaction degree	0.71

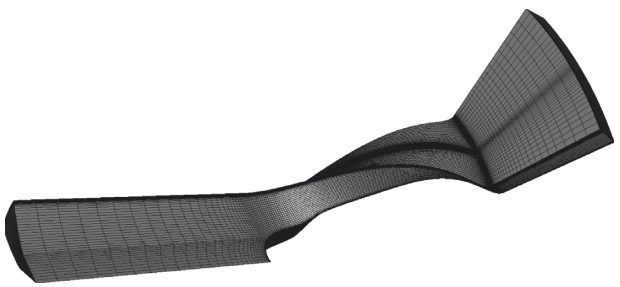

Figure 14: Computational grid of the IET supercritical CO_2 impeller.

$$\phi_{in} = \frac{\dot{V}_0}{1/4\pi D_2^2 U_2} = \frac{4\dot{m}}{\pi \rho_0 D_2^2 U_2}. \tag{31}$$

$$\psi_s = \frac{\Delta h_s}{U_2^2} = \frac{M\omega\eta}{\dot{m}U_2^2}. \tag{32}$$

The deviations between the CFD and experimental results should be acceptable as far as the compressor efficiency and the fluid enthalpy rise are concerned. The good agreement gives confidence to the numerical simulation of the IET compressor.

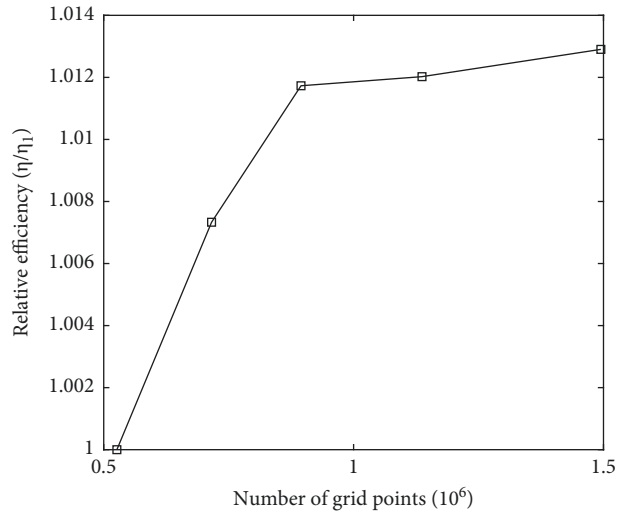

Figure 15: Grid sensitivity of the IET supercritical CO_2 centrifugal compressor.

4. Cases Study by the SNL Compressor

The 3 cases were simulated with the same numerical scheme and solver but different inlet boundary conditions and rotating speeds. The ideal gas model is used in Case 1 because it is far away from the critical point. The real-gas model was used for the simulations of Case 2 and Case 3. In Cases 1–3, the boundary conditions and rotational speeds were readjusted to maintain the machine Mach number and the Reynolds number unchanged. The difference between the three reference cases is only the inlet isentropic exponent change. Based on the similarity criteria, the rotating speed and diameters are displayed in Table 5.

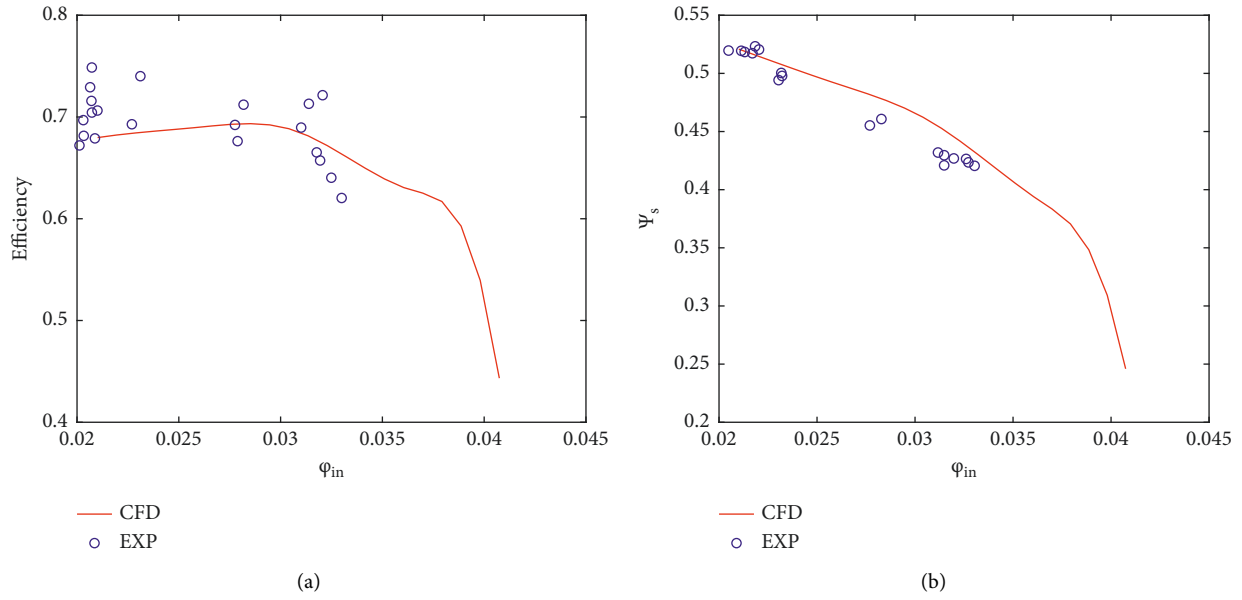

Figure 16: Comparison of numerically predicted results against the IET-CAS experimental data. (a) Compressor efficiency and (b) isentropic work coefficient.

Table 5: Settings of the SNL reference cases.

No.	Fluid	T_0 (K)	P_0 (kPa)	D_2 (m)	N (RPM)	Re_M (E)	Ma_M	n_s
Case 1	Ideal gas	288.15	500	0.55	6173.7	6.367	0.681	1.29
Case 2	Real gas	306.8	7730	0.03736	62910	6.367	0.681	1.57
Case 3	Real gas	305	8100	0.0275	124810	6.367	0.681	5.74

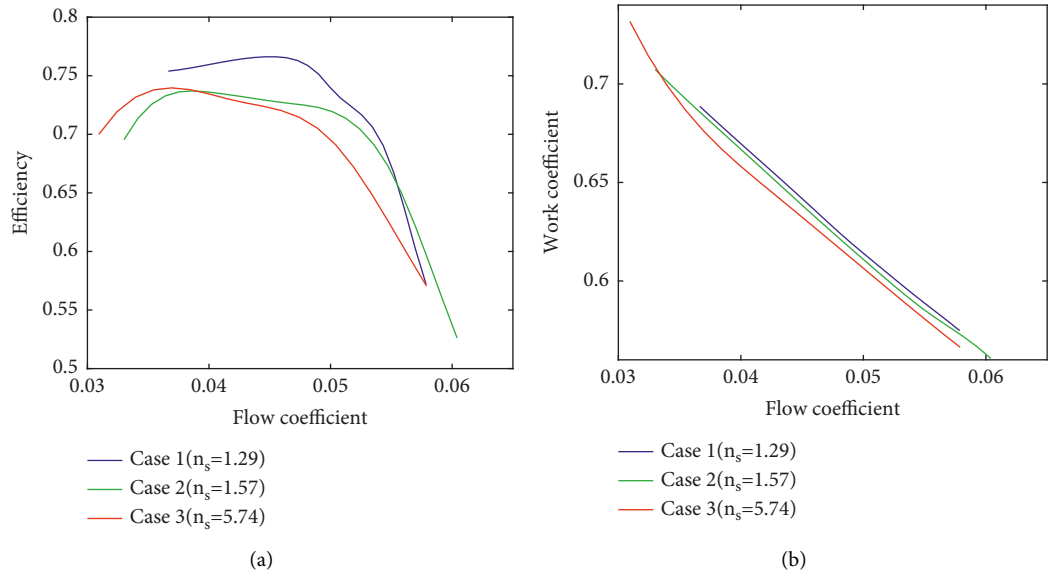

Figure 17: Dimensionless compressor characteristics. (a) Efficiency and (b) work coefficient.

4.1. Effects on the Performance Map. The real-gas effect on the compressor performance is a great concern for a supercritical CO_2 cycle design. For a small-sized supercritical CO_2 compressor, a few laboratories successfully conducted physical experiments. However, for a large-sized supercritical CO_2 compressor, the requirement of power driving the compressor is so high that most laboratories cannot afford it. Therefore, the difficulty in the physical experiment conduction is a serious issue that the development of the supercritical CO_2 compressor has to address. As an alternative approach to solving the issue, dimensionless compressor characteristics can simplify

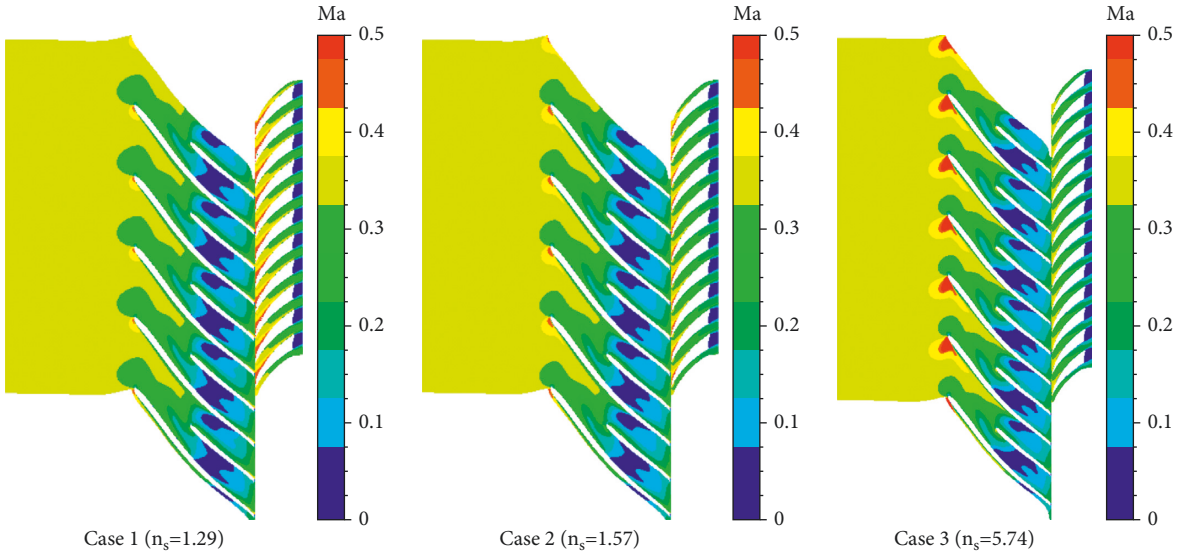

Figure 18: Mach number distribution of test cases (at 85% span).

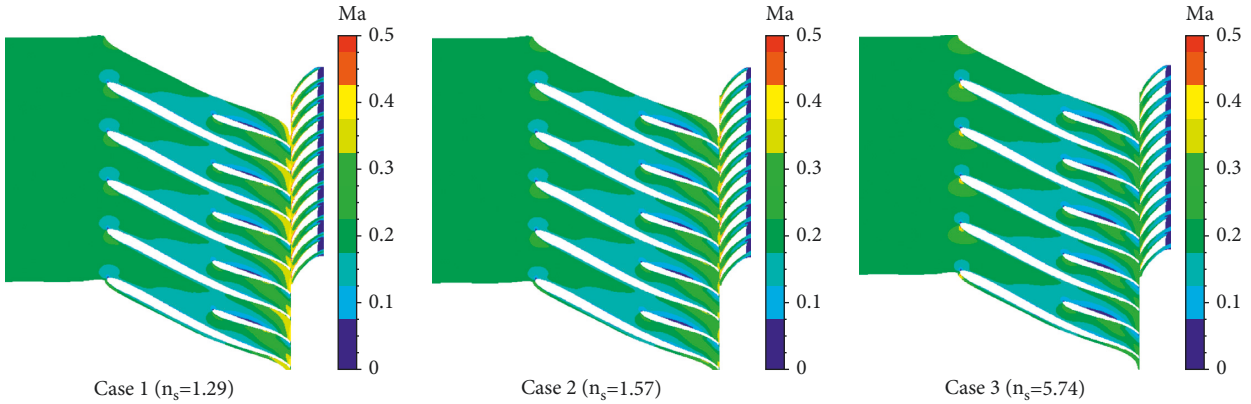

Figure 19: Mach number distribution of test cases (at 15% span).

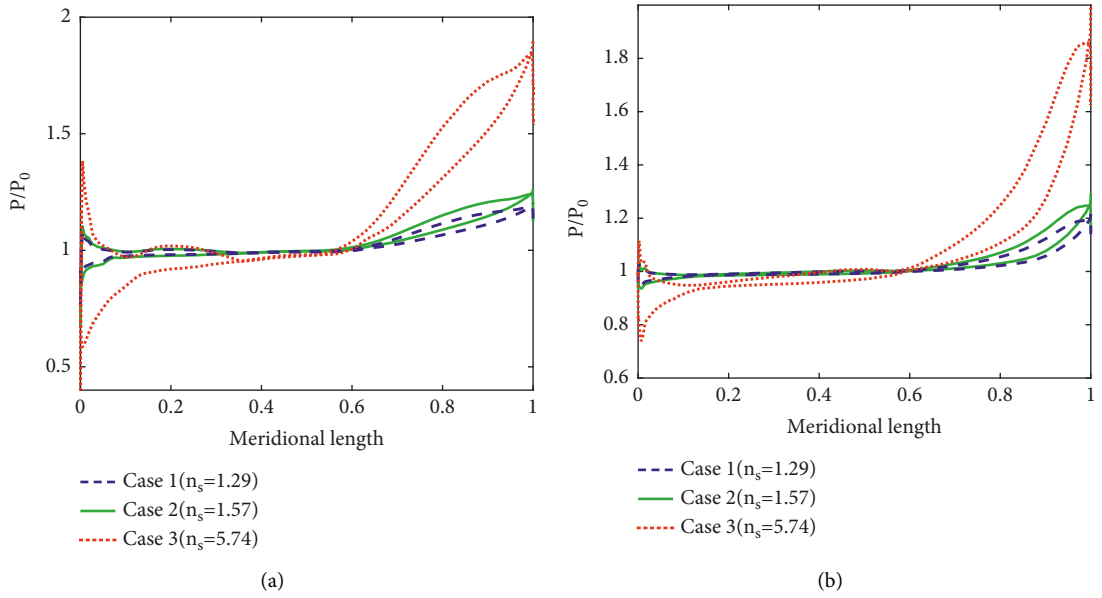

Figure 20: Dimensionless pressure along the impeller meridional direction. (a) At the span of 85%. (b) At the span of 15%.

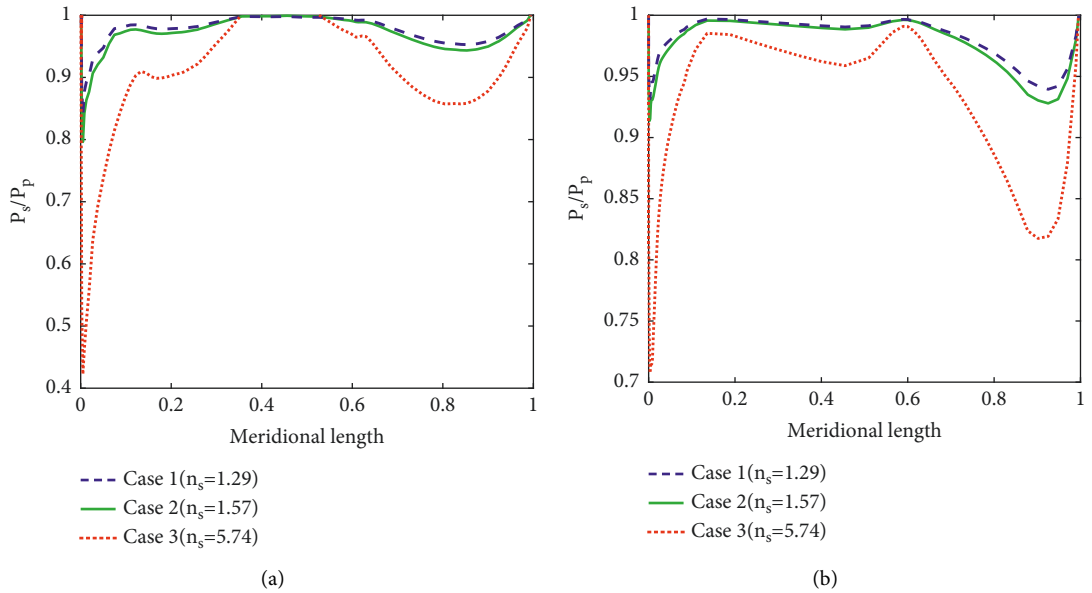

Figure 21: P_s/P_p along the impeller meridional direction. (a) At the span of 85%. (b) At the span of 15%.

Table 6: Settings of the reference cases.

No.	Fluid	T_0 (K)	P_0 (kPa)	D_2 (m)	N (RPM)	Re_M (E)	Ma_M	n_s
Case 1	Ideal gas	288.15	500	1.814	1809	2.048	0.659	1.29
Case 2	Real gas	307	7800	0.124	18047	2.048	0.659	1.62
Case 3	Real gas	307	8347	0.096	32000	2.048	0.659	4.52

the physical experiment and mitigate the test difficulty. The performance maps of Cases 1–3 are illustrated in Figure 17 using the numerical method validated in Section 3.

The work coefficient deviation between Case 1 and 2 is not too large. The main reason is the similar inlet isentropic exponents. However, Case 3 shows a considerable deviation for Case 1, not only on the efficiency but also the work coefficient. The mechanism contributing to those deviations is increasing the isentropic exponent value from 1.29 in Case 1 to 5.74 in Case 3. This follows the theoretical prediction (Section 2.2) that the larger inlet isentropic exponent is, the lower work coefficient is. The consistency supports the theoretical analysis.

4.2. Effects on the Internal Flow. As a typical and valuable dimensionless parameter, the Mach number can reflect the compressibility of working fluid. Figures 18 and 19 show the Mach number distributions at 85% and 15% spans (ϕ = 0.05), respectively. It can be seen that the Mach number of real-gas cases (Case 2 and Case 3) at the leading edge suction side is higher than ideal one (Case 1). Moreover, the larger the inlet isentropic exponent, the higher the Mach number is at the leading edge suction side. At the impeller outlet, Figure 18 also shows a lower Mach number of real-gas cases (Case 2 and Case 3) than the ideal gas case (Case 1). In addition, the larger the inlet isentropic exponent is, the lower the Mach number at the

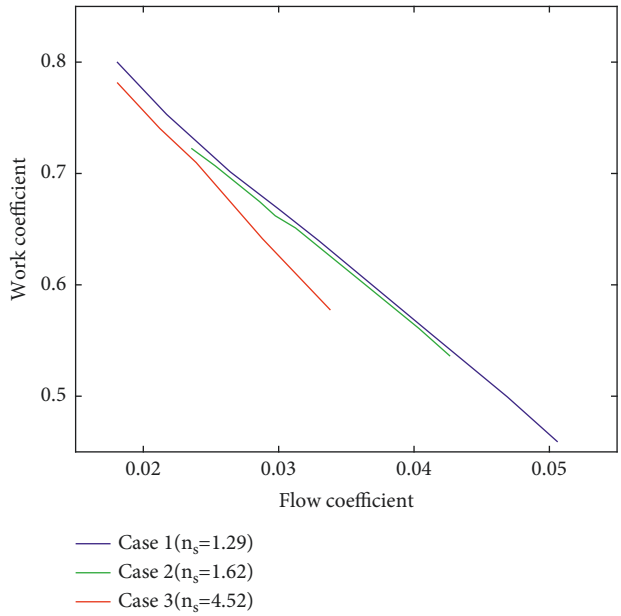

Figure 22: Work coefficient of test cases.

impeller outlet is. Those findings derived from the CFD simulations entirely agree with the aerodynamic analysis stated in Section 2.3, thus supporting the theoretical analysis.

Figure 20 presents the dimensionless pressure along the meridional direction. The pressure is obtained under the

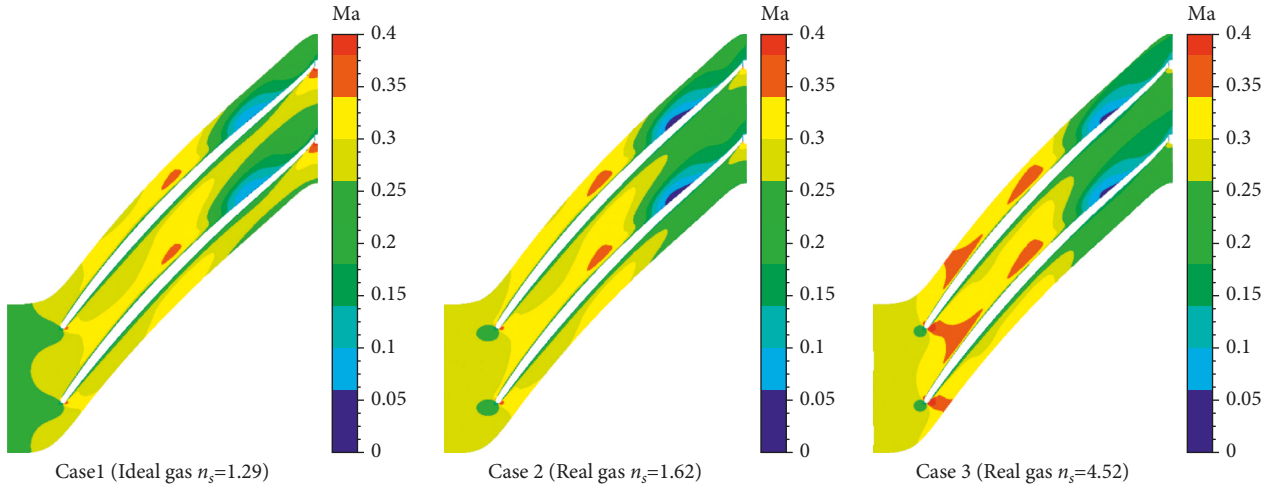

Figure 23: Mach number distribution of test cases (at 50% span).

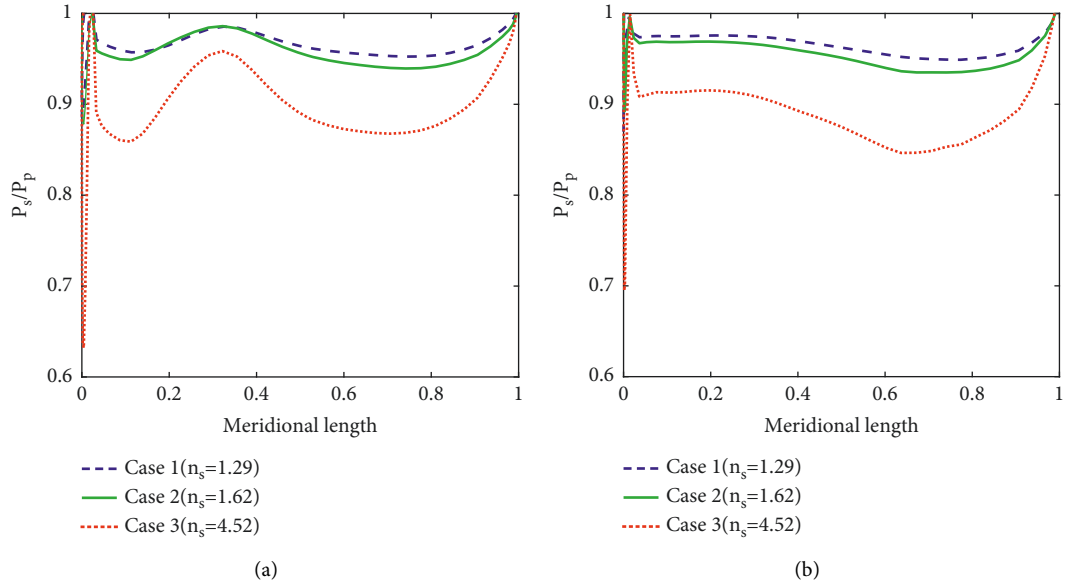

Figure 24: P_s/P_p along the impeller meridional length. (a) At 85% of the span. (b) At 15% of the span.

similarity conditions shown in Table 4. A slight deviation is found at the leading edge and the trailing edge between Case 1 and Case 2. As for Case 3, the dimensionless pressure at the trailing edge is much higher than that in other cases. This result agrees with the theoretically predicted result in Section 2.1. The higher the inlet isentropic exponent, the higher the dimensionless pressure is, especially at the impeller outlet.

The ratio of static pressure values on two sides of a blade can indicate the local blade loading. Figure 21 shows the P_s/P_p along the impeller meridional line. Slight differences occur between Case 1 and Case 2 and exhibit an insignificant influence on the blade loading. However, Case 3 shows a remarkable isentropic exponent effect on the blade loading. It is found that the P_s/P_p of Case 3 near the leading/trailing edge is much lower than that in other cases. The finding is still consistent with theoretical prediction, thus supporting the theoretical analysis.

In conclusion, the analysis mentioned above indicates that the performance of a supercritical CO_2 compressor is related to the inlet isentropic exponent. Specifically, increasing the isentropic exponent will reduce the work coefficient. Besides the performance, the inlet isentropic exponent has a significant impact on the impeller flow field. Specifically, the higher inlet isentropic exponent would increase the Mach number and blade loading at the leading edge of the impeller, but decrease the Mach number at the impeller outlet.

5. Cases Study by the IET Compressor

An additional validation was carried out with the IET supercritical CO_2 compressor. The machine Mach number and machine Reynolds number are maintained to be the same in the simulations. Under similar conditions,

the rotating speeds and diameters are displayed in Table 6.

Figure 22 presents the performance of the MWe scale supercritical CO_2 compressor. It can be found that the higher inlet isentropic exponent case shows a lower work coefficient.

Figure 23 displays the Mach distribution of the MWe scale supercritical CO_2 compressor at 50% span ($\phi = 0.03$). It can be confirmed that the higher inlet isentropic exponent case shows a higher Mach number at the leading edge and a lower Mach number at the trailing edge.

The blade loading (P_s/P_p) of the MWe scale supercritical CO_2 compressor is displayed in Figure 24. It can be concluded that the higher inlet isentropic exponent case has a higher loading.

In short, this section validates the theoretical prediction according to the numerical simulations on the IET compressor. The numerical results reveal that the isentropic exponent affects the work coefficient, Mach number, and blade loading. The effects are consistent with the theoretical prediction, thus supporting the core part of this paper, the theoretical analysis.

6. Conclusion

This paper investigated the isentropic exponent effects on the flow similarity in supercritical CO_2 compressors. The main concerns are compressor performance and flow field. The investigation method includes both three-dimensional CFD simulations and theoretical analyses. Based on the discussion stated in this paper, the main conclusions and a suggestion for the future physical test are stated as follows:

(1) In a 3D impeller, the isentropic exponent plays a role in the performance of compressors with supercritical CO_2 as its working fluid, especially for large isentropic exponent cases (near the CO_2 critical point). The increase in isentropic exponent tends to decrease the impeller work coefficient.

(2) The inlet isentropic exponent has a significant impact on the impeller flow field. The increase in the inlet isentropic exponent increases the Mach number and blade loading at the leading edge of the impeller blade but decreases the Mach number at the impeller outlet.

(3) The inlet isentropic exponent fluctuation has to be considered in a physical experiment of a centrifugal compressor with supercritical CO_2 as its working fluid. During designing a test of this sort, it is suggested to assess the inlet isentropic exponent fluctuation and then ensure its fluctuating range to meet the requirements of the flow similarity.

Abbreviations

a: Sound speed
c: Specific heat capacity
D: Diameter
h: Specific enthalpy
$\dot{m}$: Mass flow rate
Ma: Mach number
m: Meridional length
M: Torque
N: Shaft speed
P: Pressure
r: Gas constant (for CO2, 188.97 J/(kg·K)), radius
T: Temperature
U: Circumferential velocity
V: Absolute velocity in diffuser
W: Relative velocity
Z: Compressibility factor.

Appendix

A. Effects on the Density and Pressure

When the inlet parameters are specified, both the static enthalpy and the relative velocity at an arbitrary location in the turbomachinery meet the following relationship:

$$\frac{h_x + W_x^2/2 - U_x^2}{2} = \frac{h_1 + W_1^2/2 - U_1^2}{2} = h_0. \tag{A.1}$$

Assuming the process is isentropic and with the equation of state, the density, pressure, and local sound speed can be determined by enthalpy and entropy. Since the inlet entropy and stagnation enthalpy are input parameters, the local state parameters are determined by the local velocity magnitude. Specifically, the local density is expressed herein.

$$\begin{aligned}\frac{\rho_x}{\rho_0} &= \left(\frac{T_x}{T_0}\right)^{1/(n_s-1)} = \left(\frac{h_x}{h_0}\right)^{1/(n_s-1)} \\ &= \left(\frac{h_0 + U_x^2/2 - W_x^2/2}{h_0}\right)^{1/(n_s-1)} \\ &= \left[1 + \frac{1}{2}\left(\frac{U_x}{U_2}\right)^2 \frac{U_2^2}{h_0} - \frac{1}{2}\frac{W_x}{h_x}\frac{h_x}{h_0}\right]^{1/(n_s-1)}.\end{aligned} \tag{A.2}$$

The rest of the derivation process converts the local velocity into the local Mach number. The following equation describes the relationship between the ideal gas enthalpy and the sound speed.

$$h = \frac{n_s}{n_s - 1} RT = \frac{a^2}{n_s - 1}. \tag{A.3}$$

Substitute (A.3) into (A.2).

$$\frac{\rho_x}{\rho_0}=\left[1+\frac{n_s-1}{2}\left(\frac{U_x}{U_2}\right)^2 Ma_M^2-\frac{n_s-1}{2}Ma_x^2\left(1+\frac{n_s-1}{2}Ma_x^2-\frac{n_s-1}{2}Ma_{ux}^2\right)^{-1}\right]^{1/(n_s-1)}. \tag{A.4}$$

Similarly, an expression about the pressure can be derived. The following relationship exists between the unknown local circumferential Mach number and the machine Mach number:

$$\begin{aligned}&\frac{Ma_{ux}}{Ma_M}\\&=\frac{U_x}{U_2}\left(\frac{h_x+W_x^2/2-U_x^2/2}{h_x}\right)^{1/2}\\&=\frac{U_x}{U_2}\left(1+\frac{n_s-1}{2}Ma_x^2-\frac{n_s-1}{2}Ma_{ux}^2\right)^{1/2}.\end{aligned} \tag{A.5}$$

For the real gases, the isentropic calculation is carried out by looking up the real-gas property table.

$$\frac{\rho_x}{\rho_0}=\frac{\rho(h_x,s_0)}{\rho_0}=\frac{\rho\left(h_0+U_x^2/2-W_x^2/2,s_0\right)}{\rho_0}, \tag{A.6}$$

$$\frac{P_x}{P_0}=\frac{P(h_x,s_0)}{P_0}=\frac{P\left(h_0+U_x^2/2-W_x^2/2,s_0\right)}{P_0}, \tag{A.7}$$

$$Ma_x=\frac{W_x}{a_x}=\frac{W_x}{a(h_x,s_0)}=\frac{W_x}{a\left(h_0+U_x^2/2-W_x^2/2,s_0\right)}. \tag{A.8}$$

B. Effects on the Impeller Outlet Mach Number

For impellers, the continuity equation is generally expressed by relative velocity.

$$\frac{\rho_x}{\rho_{1,m}}\cdot\frac{W_x}{W_{1,m}}\cdot\frac{A_x}{A_1}\cdot\frac{\cos\beta_x}{\cos\beta_{1,m}}-1=0. \tag{B.1}$$

Different from the diffuser, the stagnation parameters in the impeller are variable due to the rotation and blade. According to the conservation of rothalpy, the density and sound speed at different positions in the impeller have the following relationship:

$$\frac{\rho_x}{\rho_{1,m}}=\left(\frac{h_x}{h_{1,m}}\right)^{1/(n_s-1)}=\left(\frac{h_{1,m}+W_{1,m}^2/2-U_{1,m}^2/2+U_x^2/2-W_x^2/2}{h_{1,m}}\right)^{1/(n_s-1)}, \tag{B.2}$$

$$\frac{\rho_x}{\rho_{1,m}}=\left[1+(n_s-1)\frac{1-\left(W_x/W_{1,m}\right)^2}{2}Ma_{1,m}^2+(n_s-1)\frac{\left(U_x/U_{1,m}\right)^2-1}{2}Ma_{u1,m}^2\right]^{1/(n_s-1)}, \tag{B.3}$$

Substitute (B.1) into (B.3).

$$\frac{W_x}{W_{1,m}}=\frac{A_1}{A_x}\frac{\cos\beta_{1,m}}{\cos\beta_x}\left[1+(n_s-1)\frac{1-\left(W_x/W_{1,m}\right)^2}{2}Ma_{1,m}^2+(n_s-1)\frac{\left(U_x/U_{1,m}\right)^2-1}{2}Ma_{u1,m}^2\right]^{-1/(n_s-1)}, \tag{B.4}$$

Based on the relationship between the Mach number and sound speed, the relative velocity (W_x) can be transformed into the relative Mach number (Ma_x).

$$\frac{Ma_x}{Ma_{1,m}}=\frac{W_x/W_{1,m}}{a_x/a_{1,m}}, \tag{B.5}$$

$$\frac{a_x}{a_{1,m}}=\left[1+(n_s-1)\frac{1-\left(W_x/W_{1,m}\right)^2}{2}Ma_{1,m}^2+(n_s-1)\frac{\left(U_x/U_{1,m}\right)^2-1}{2}Ma_{u1,m}^2\right]^{1/2}. \tag{B.6}$$

An undetermined parameter, $Ma_{u1,\ m}$, appears in formula (B.6). According to formula (A.5), the conversion relationship between the inlet circumference Mach number and the machine Mach number can be described as follows:

$$\frac{Ma_{u1,m}}{Ma_M} = \frac{U_{1,m}}{U_2}\left(1 + \frac{n_s - 1}{2} Ma_{1,m}^2 - \frac{n_s - 1}{2} Ma_{u1,m}^2\right)^{1/2}. \tag{B.7}$$

In the impeller, the flow coefficient can be expressed as follows:

$$\phi = \frac{D_{s1}^2 - D_{h1}^2}{D_2^2} \frac{Ma_{1,m}}{Ma_M} \frac{\rho_1}{\rho_0} \frac{a_1}{a_0} \cos\beta_{1,m}. \tag{B.8}$$

C. Leading Edge Mach Number

The relative velocity difference between the two sides of an impeller blade approximately satisfies the following equation under a small attack angle condition [40].

$$\frac{W_{x,s} - W_{x,p}}{r_x \Delta\theta_x} + W_x \frac{\cos\beta_x \sin\beta_x}{\rho_x b_x} \frac{d\rho\ b}{dm}\Big|_x. \tag{C.1}$$

It can be seen from the above formula that the blade loading is composed of three parts and the presented research shows that the contribution of the third term to the blade load is tiny and thus can be ignored [41]. Therefore, it can be simplified as follows:

$$\frac{W_{x,s} - W_{x,p}}{W_x} = 2\frac{U_x}{W_x} \sin\gamma_x \cos\beta_x \Delta\theta_x - \frac{r\ d\beta}{dm}\Big|_x \Delta\theta_x. \tag{C.2}$$

At the tip of the impeller leading edge, the inclination angle of the streamline is 0. Thus, it can be simplified further as follows:

$$\frac{\Delta W_{1t}}{W_{1t}} = -\frac{r\ d\beta}{dm}\Big|_{1t} \Delta\theta_1. \tag{C.3}$$

Usually, $d\beta/dm|_{1t} < 0$. The relative velocity at the suction and pressure surface can be derived from the velocity difference.

$$W_{1t,p} = W_{1t} - \frac{\Delta W_{1t}}{2} = W_{1t}\left(1 + \frac{r\ d\beta}{2\ dm}\Big|_{1t} \Delta\theta_1\right), \tag{C.4}$$

$$W_{1t,s} = W_{1t} + \frac{\Delta W_{1t}}{2} = W_{1t}\left(1 - \frac{r\ d\beta}{2\ dm}\Big|_{1t} \Delta\theta_1\right). \tag{C.5}$$

Thus, the Mach numbers of the blade suction and pressure surfaces near the leading edge can be expressed as follows:

$$Ma_{1t,s} = Ma_{1t}\left(1 - \frac{r\ d\beta}{2\ dm}\Big|_{1t} \Delta\theta_1\right), \tag{C.6}$$

$$Ma_{1t,p} = Ma_{1t}\left(1 + \frac{r\ d\beta}{2\ dm}\Big|_{1t} \Delta\theta_1\right), \tag{C.7}$$

Greek Symbols

β: Flow angle
ρ: Density
ω: Angular velocity
η: Efficiency
ϕ: Flow coefficient
μ: Dynamic viscosity
γ: Specific heat ratio (Cp/Cv)

Subscripts

0: Stagnation condition in absolute coordinate
1: Impeller inlet
2: Impeller outlet
ad: Dimensionless parameter
cr: Critical conditions (calculated by equation 28 and 29)
M: Machine parameters
m: Average parameters
p: Pressure side
s: Isentropic process, suction side
t: Tip
u: Circumferential direction
x: Arbitrary position in the impeller.

Data Availability

No other underlying data were used to support this study.

Conflicts of Interest

The authors declare that they have no potential conflicts of interest with respect to the research, authorship, and/or publication of this article.

Acknowledgments

This work was financially supported by the National Natural Science Foundation of China (Grant no. 52006217). The authors want to thank Prof. Yuyan Jiang (now in Beijing Institute of Technology) and Dr. Yuming Zhu from the Institute of Engineering Thermophysics-Chinese Academy of Sciences for providing the measurement data.

References

[1] E. G. Feher, "The supercritical thermodynamic power cycle," *Energy Conversion*, vol. 8, no. 2, pp. 85–90, 1968.
[2] G. Angelino, "Real gas effects in carbon dioxide cycles," in *Proceedings of the ASME 1969 Gas Turbine Conference and Products Show*, Cleveland, OH, USA, March 1969.
[3] Z. Liu, P. Wang, X. Sun, and B. Zhao, "Analysis on thermodynamic and economic performances of supercritical

carbon dioxide Brayton cycle with the dynamic component models and constraint conditions," *Energy*, vol. 240, Article ID 122792, 2022.

[4] Z. Liu, Z. Li, Y. Zhang, Y. Zhang, and B. Zhao, "Thermodynamic analysis of using chemical-looping combustion in Allam-Z cycle instead of common combustion," *Energy Conversion and Management*, vol. 254, Article ID 115229, 2022.

[5] H. Li, G. Fan, L. Cao et al., "A comprehensive investigation on the design and off-design performance of supercritical carbon dioxide power system based on the small-scale lead-cooled fast reactor," *Journal of Cleaner Production*, vol. 256, Article ID 120720, 2020.

[6] J. Xu, C. Liu, E. Sun et al., "Perspective of S–CO_2 power cycles," *Energy*, vol. 186, Article ID 115831, 2019.

[7] H. Li, M. Wang, J. Wang, and Y. Dai, "Exergoeconomic analysis and optimization of a supercritical CO_2 cycle coupled with a Kalina cycle," *Journal of Energy Engineering*, vol. 143, no. 2, Article ID 04016055, 2017.

[8] Y. Zhang, H. Li, W. Han et al., "Improved design of supercritical CO_2 Brayton cycle for coal-fired power plant," *Energy*, vol. 155, pp. 1–14, 2018.

[9] V. Dostal, P. Hejzlar, and M. J. Driscoll, "High-performance supercritical carbon dioxide cycle for next-generation nuclear reactors," *Nuclear Technology*, vol. 154, no. 3, pp. 265–282, 2006.

[10] P. Garg, P. Kumar, and K. Srinivasan, "Supercritical carbon dioxide Brayton cycle for concentrated solar power," *The Journal of Supercritical Fluids*, vol. 76, pp. 54–60, 2013.

[11] F. G. Battisti, G. S. Delsoto, and A. K. da Silva, "Transient analysis and optimization of a recuperative sCO_2 Brayton cycle assisted by heat and mass storage systems," *Energy*, vol. 150, pp. 979–991, 2018.

[12] Z. Liu, W. Luo, Q. Zhao, W. Zhao, and J. Xu, "Preliminary design and model assessment of a supercritical CO_2 compressor," *Applied Sciences*, vol. 8, no. 4, p. 595, 2018.

[13] Z. Liu, Q. Zhao, X. Xiang, W. Zhao, and X. Zhou, "A hybrid viscous body force model for low-speed centrifugal compressors," *Proceedings of the Institution of Mechanical Engineers, Part A: Journal of Power and Energy*, vol. 235, no. 3, pp. 335–350, 2021.

[14] M. Utamura, T. Fukuda, and M. Aritomi, "Aerodynamic characteristics of a centrifugal compressor working in supercritical carbon dioxide," *Energy Procedia*, vol. 14, pp. 1149–1155, 2012.

[15] E. M. Clementoni and T. L. Cox, "Steady-state power operation of a supercritical carbon dioxide Brayton cycle," in *Proceedings of the ASME Turbo Expo 2014: Turbine Technical Conference and Exposition*, Düsseldorf, Germany, 2014 September.

[16] G. Dufour, X. Carbonneau, J. B. Cazalbou, and P. Chassaing, "Practical use of similarity and scaling laws for centrifugal compressor design," in *Proceedings of the Turbo expo: power for Land, Sea, and Air*, pp. 1131–1140, Barcelona, Spain, 2006 January.

[17] S. A. Wright, T. M. Conboy, and G. E. Rochau, *Supercritical CO2 Power Cycle Development Summary at Sandia National Laboratories (No. SAND2011-6640C)*, Sandia National Laboratories, Albuquerque, NM, USA, 2011.

[18] B. Monje, D. Sánchez, R. Chacartegui, T. Sánchez, M. Savill, and P. Pilidis, "Aerodynamic analysis of conical diffusers operating with air and supercritical carbon dioxide," *International Journal of Heat and Fluid Flow*, vol. 44, pp. 542–553, 2013.

[19] C. Tello, A. Muñoz, D. Sánchez, T. Kipouros, and M. Savill, "Impact of fluid substitution on the performance of an axial compressor blade cascade working with supercritical carbon dioxide," *Journal of Engineering for Gas Turbines and Power*, vol. 142, no. 1, 2020.

[20] N. D. Baltadjiev, C. Lettieri, and Z. S. Spakovszky, "An investigation of real gas effects in supercritical CO_2 centrifugal compressors," *Journal of Turbomachinery*, vol. 137, no. 9, 2015.

[21] A. Romei, P. Gaetani, and G. Persico, "On sCO_2 compressor performance maps at variable intake thermodynamic conditions," in *Proceedings of the Turbo Expo: Power for Land, Sea, and Air*, New York, NY, USA, June 2021.

[22] H. S. Pham, N. Alpy, J. H. Ferrasse et al., "An approach for establishing the performance maps of the sc-CO_2 compressor: development and qualification by means of CFD simulations," *International Journal of Heat and Fluid Flow*, vol. 61, pp. 379–394, 2016.

[23] Y. Jeong, S. Son, S. K. Cho, S. Baik, and J. I. Lee, "Evaluation of supercritical CO_2 compressor off-design performance prediction methods," *Energy*, vol. 213, Article ID 119071, 2020.

[24] B. Zhao, C. Yang, L. Hu et al., "Understanding of the interaction between clearance leakage flow and main passage flow in a VGT turbine," *Advances in Mechanical Engineering*, vol. 7, no. 2, Article ID 652769, 2015.

[25] Z. Tian, Q. Zheng, P. Liu, A. Malik, and B. Jiang, "Effect of shroud end wall structure on tip leakage flow in highly loaded helium compressor rotor," *Energy*, vol. 179, pp. 1114–1123, 2019.

[26] F. R. Menter, M. Kuntz, and R. Langtry, "Ten years of industrial experience with the SST turbulence model," *Turbulence, Heat and Mass Transfer*, vol. 4, no. 1, pp. 625–632, 2003.

[27] J. D. Denton, "The Calculation of three-dimensional viscous flow through multistage turbomachines," *The Journal of Turbomachinery*, vol. 144, 1992.

[28] X. Li, Y. Zhao, H. Yao, M. Zhao, and Z. Liu, "A new method for impeller inlet design of supercritical CO_2 centrifugal compressors in Brayton cycles," *Energies*, vol. 13, no. 19, Article ID 5049, 2020.

[29] S. Saxena, R. Mallina, F. Moraga, and D. Hofer, "Numerical approach for real gas simulations: Part II—flow simulation for supercritical CO_2 centrifugal compressor," in *Proceedings of the Turbo Expo: Power for Land, Sea, and Air*, Charlotte, NC, USA, June 2017.

[30] T. Conboy, S. Wright, J. Pasch, D. Fleming, G. Rochau, and R. Fuller, "Performance characteristics of an operating supercritical CO_2 Brayton cycle," *Journal of Engineering for Gas Turbines and Power*, vol. 134, no. 11, 2012.

[31] S. A. Wright, R. F. Radel, M. E. Vernon, G. E. Rochau, and P. S. Pickard, *Operation and Analysis of a Supercritical CO_2 Brayton Cycle*, Sandia National Laboratories, Albuquerque, NM, and Livermore, CA USA, 2010.

[32] Y. Zhu, "Study on supercritical carbon dioxide centrifugal compressor," doctoral dissertation, University of Chinese Academy of Sciences, Huairou District, China, 2020.

[33] S. Raman and H. Kim, "Computational analysis of the performance characteristics of a supercritical CO_2 centrifugal compressor," *Computation*, vol. 6, no. 4, p. 54, 2018.

[34] A. Ameli, T. Turunen-Saaresti, and J. Backman, "Numerical investigation of the flow behavior inside a supercritical CO_2 centrifugal compressor," in *Proceedings of the ASME Turbo Expo 2016: Turbomachinery Technical Conference and Exposition*, Seoul, Republic of Korea, September 2016.

[35] A. J. Glassman, *Turbine Design and Application*, Scientific and Technical Information Office, National Aeronautics and Space Administration, Hampton, VA, 1972.

[36] Y. Zhu and S. A. Sjolander, "Effect of geometry on the performance of radial vaneless diffusers," *Journal of Turbomachinery*, vol. 109, no. 4, pp. 550–556, 1987.

[37] R. H. Aungier, *Axial-flow Compressors-A Strategy for Aerodynamic Design and Analysis*, The American Society of Mechanical Engieers, New York, NY, USA, 2003.

[38] H. W. Oh, E. S. Yoon, and M. K. Chung, "An optimum set of loss models for performance prediction of centrifugal compressors," *Proceedings of the Institution of Mechanical Engineers, Part A: Journal of Power and Energy*, vol. 211, no. 4, pp. 331–338, 1997.

[39] J. W. Daily and R. E. Nece, "Chamber dimension effects on induced flow and frictional resistance of enclosed rotating disks," *Journal of Fluids Engineering*, vol. 82, 1960.

[40] N. A. Cumpsty, *Compressor Aerodynamics*, Longman Scientific and Technical, Harlow, UK, 1989.

[41] C. Zhang, X. Dong, X. Liu, Q. Gao, C. Tan, and D. Zeng, "One-dimensional modeling for tip clearance leakage vortex trajectory and stall-onset prediction in subsonic centrifugal impellers," *Proceedings of the Institution of Mechanical Engineers, Part A: Journal of Power and Energy*, vol. 234, no. 3, pp. 263–282, 2020.